RESEARCH PAPER

Static and dynamic behaviour of gas bubbles in T-shaped non-clogging micro-channels

C. Litterst · T. Metz · R. Zengerle ·
P. Koltay

Abstract Preventing micro-channels from clogging is a major issue in most micro and nanofluidic systems (Gravesen et al., J Micromech Microeng 3(4):168–182, 1993; Jensen et al., In: Proc. of MicroTAS 2002, Nara, Japan, pp 733–735, 2002; Wong et al., J Fluid Mech 292:71–94, 1995). The T-shaped channel first reported by Kohnle et al. (In: IEEE MEMS, the 15th international IEEE micro electro mechanical conference (ed), Las Vegas, pp 77–80, 2002) prevents micro-channels from clogging by the aid of the equilibrium bubble position in such a geometry. This work is concerned with the static and dynamic behaviour of bubbles in such T-shaped micro-channels. The aspect ratio of a rectangle enclosing the T-shaped channel and the contact angle of the walls are the main parameters influencing the static and dynamic bubble behaviour. It is investigated in this article how these parameters relate to the equilibrium bubble shape and how optimum bubble velocities can be achieved inside the channel. An analytical model depending on the contact angle and the channel geometry is presented that allows to determine the bubble configuration inside the channel by minimizing the bubble's surface energy. A second model is derived to predict the velocity of gas bubbles driven by buoyancy in vertical T-shaped channels. The model is applied to design T-shaped channels with a maximum mobility of gas bubbles. Experiments with MEMS fabricated devices and CFD simulations are used to verify the models. Furthermore design rules for an optimum non-clogging channel geometry which provides the highest gas bubble mobility are given.

List of symbols

b_h	width of the horizontal channel
b_v	height of the vertical channel
a_h	height of the horizontal channel
a_v	width of the vertical channel
E_{tot}	total interfacial energy
g	ground acceleration (9.81 m s^{-1})
l_{bub}	length of a gas bubble
V_{bub}	volume of a gas bubble
A	plain area, e.g. channel or bubble cross-section
S	surface area, e.g. surrounding a bubble
$\bar{v}$	bubble rise velocity
θ	contact angle
ρ	density (water: 1,000 kg m^{-3})
η	dynamic viscosity (water: 0.001 Pa s)
σ	surface tension (water: 0.0727 N m^{-1})
Φ_i	flow rate of the medium i

Indices

lg	liquid–gas interface
sl	solid–liquid interface
sg	solid gas interface
h	horizontal
v	vertical
c	clogged

C. Litterst (✉) · T. Metz · R. Zengerle · P. Koltay
Laboratory for MEMS Applications, Department of
Microsystems Engineering (IMTEK), University of Freiburg,
Georges-Koehler-Allee 106, 79110 Freiburg, Germany
e-mail: litterst@imtek.de
URL: www.imtek.de/anwendungen

R. Zengerle
e-mail: roland.zengerle@imtek.uni-freiburg.de

1 Introduction

It is a well known phenomena in micro-fluidics that gas bubbles are able to block liquid flow in micro-channels (Gravesen et al. 1993). Reasons for this are the pressure loss from front menisci to back menisci of bubbles due to contact angle dynamics (Wong et al. 2005) and constrictions (Jensen et al. 2004). Apart from blocking channels from liquid flow entrapped bubbles can act by their compressibility as capacitive elements which lead to a damping of high frequent flow signals that are required, e.g. in micro-pumps or dispensers (Steinert et al. 2004).

Some strategies exist to avoid the inclusion of gas bubbles at initial priming of micro-fluidic systems (Goldschmidtboeing et al. 2006; Steinert et al. 2004; Zengerle et al. 1995) which may not be applicable in all cases. In particular these strategies fail if bubbles occur in micro-fluidic systems during the normal operation of a device like, e.g. in direct methanol fuel cells (Litterst et al. 2006) or electrolysers. The T-shaped channels studied in this work provide another approach to the described problem: the idea is to guide existing bubbles into positions where they do not disturb the micro-fluidic process or where they can be discharged from the device. This is achieved by geometrical constraints of the channel walls only without changing the wetting conditions.

The structure sketched in Fig. 1 has been presented first in Kohnle et al. (2002), where it was termed channel in channel (CHIC). In the current work it will be referred to as T-shaped channel. The channel design is built by a horizontal and a vertical block parameterized by $a_h b_h$ and $a_v b_v$. Therefore the outer dimensions of the rectangle enclosing the channel cross-section is given by the parameters $b_h b_v$.

The design avoids complete obstruction (clogging) of the channel by gas bubbles and improves their mobility under certain circumstances. Its practical applicability has been demonstrated in a highly integrated sensor controlled fountain pen (Waibel et al. 2003) as well as in a flow field for the removal of gas bubbles from the anode side of a direct methanol fue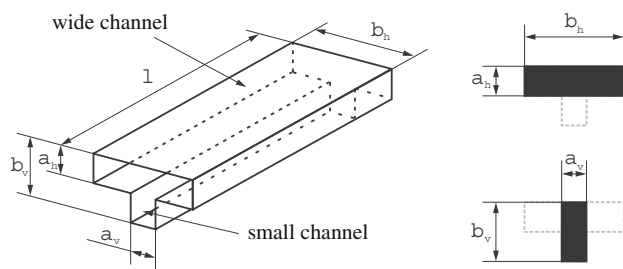l cell (Litterst et al. 2006). The channel configuration can be produced simply by a two step etching process or micro-milling.

In a well designed T-shaped channel an entrapped gas bubble either adopts a vertical or horizontal shape only covering the channel cross-section partially. This leads to either two or one liquid filled spaces beside a bubble (Fig. 2a, c) where liquid can bypass. If a T-shaped channel is not well designed, a gas bubble can also occupy the channels whole cross-section (cf. Fig. 2b). Design rules for channels leading to safe and stable bubble positions are given in section two of this work.

The bubble configurations attainable in a T-shaped channel are referred to as vertical (v), clogged (c) and horizontal (h) motivated by the projection of the bubble if observed along the channel as depicted in Fig. 2.

In the third section of this work a refined model for the mobility of the gas bubbles is presented following the approach proposed in Kohnle et al. (2002). The refined model now combines the calculation of the mobility with the prediction of the bubble configuration. The model is derived in the context of buoyancy driven bubble raise and verified by experiments.

2 Prediction of bubble configurations

The actual shape of a bubble in a micro-channel is a consequence of the system's effort to minimize interfacial energy. Thus, apart from using a software like Surface Evolver (2008) or a CFD-software tool (CFD-ACE+ 2004) an estimation of the interfacial energy can be used to predict the configuration of a bubble in a T-shaped channel. Another constraint for gas bubbles at rest is a constant pressure inside the bubble resulting in an interface of constant curvature between liquid and gas (Finn 1986). The latter approach is used in Wong et al. (1992) to predict cross-sectional areas of bubbles in polygonal channels. Here the energy approach is followed as it allows for the implication of different contact angles and bubble volumes without knowing all details of the attained shape.
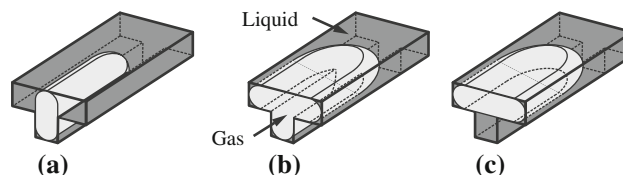

Fig. 1 Sketch of two nested channels forming a T-shaped channel and definition of the geometrical parameters. The enclosing rectangle is characterized by the parameter pair b_h and b_v

Fig. 2 Possible bubble configurations: **a** vertical; **b** clogged and **c** horizontal

2.1 Surface energy balance

The total interfacial energy E_{tot} of a liquid filled micro-channel containing a gas bubble is given by the sum of all interfacial energies in the system. These can be calculated as the product of interfacial tensions and areas:

$$E_{\text{tot}} = S_{\text{lg}}\sigma_{\text{lg}} + S_{\text{sl}}\sigma_{\text{sl}} + S_{\text{sg}}\sigma_{\text{sg}} \qquad (1)$$

Comparing different bubble configurations in a given T-shaped channel geometry the area of the liquid to solid interface changes by the same amount and opposite sign as the area of the gas to solid interface since the total solid surface of the channels interior is fixed. Assuming an unknown maximum solid interface S_0 the liquid to solid interface can be expressed as

$$S_{\text{sl}} = S_0 - S_{\text{sg}}. \qquad (2)$$

Equation (2) can be used to rewrite the total interfacial energy like

$$E_{\text{tot}} = S_0\sigma_{\text{sl}} + S_{\text{lg}}\sigma_{\text{lg}} + S_{\text{sg}}\left(\sigma_{\text{sg}} - \sigma_{\text{sl}}\right). \qquad (3)$$

Using the well known Young equation relating the contact angle to the interfacial tensions in the three phase system solid, liquid and gas (Langbein 2002):

$$\cos\theta = \frac{\sigma_{\text{sg}} - \sigma_{\text{sl}}}{\sigma_{\text{lg}}} \qquad (4)$$

Equation (3) can be rewritten to

$$\frac{E_{\text{tot}}}{\sigma_{\text{lg}}} - S_0\frac{\sigma_{\text{sl}}}{\sigma_{\text{lg}}} = S_{\text{lg}} + S_{\text{sg}}\cos\theta. \qquad (5)$$

The second term on the left hand side of Eq. (5) is constant for any configuration. S_0 and σ_{sl} are unknown but constant. All variable parameters are at the right hand side of the expression. The Eq. (5) has the dimension of a surface. The left hand side is, except for a constant, proportional to the total interfacial energy. For simplifications it will be defined as effective surface area S_{eff}:

$$S_{\text{eff}} := \frac{E_{\text{tot}}}{\sigma_{\text{lg}}} - S_0\frac{\sigma_{\text{sl}}}{\sigma_{\text{lg}}}. \qquad (6)$$

The systems effort to minimize the total interfacial energy E_{tot} therefore is equivalent to the minimization of S_{eff}. Thus by using the substitution Eq. (6), Eq. (5) yields

$$S_{\text{eff}} = S_{\text{lg}} + S_{\text{sg}}\cos\theta. \qquad (7)$$

Equation (7) includes only the interfacial areas of the bubble S_{lg} and S_{sg} as well as the contact angle θ. Using Eq. (7) it is possible to compare different bubble configurations to decide which one implies the lowest total interfacial energy and therefore will be adopted by the system.

2.2 Shape approximation

To derive expressions for the surface areas on the right hand side of Eq. (7) the configurations of the bubbles in the T-shaped channel like shown in Fig. 2 are approximated in this work by prisms as depicted in Fig. 3 with polygonal base areas, enclosing the bubbles. This approximation is justified if the bubbles are long, i.e. their length is considerably larger than the maximum channel diameter. The base areas of the prisms are given by the gas covered cross-section of the channel part containing a gas bubble as shown in Fig. 3.

The parameterization of the T-shaped channel used here allows one to describe the cross-sectional area claimed by a bubble in the vertical or horizontal configuration using a single pair of variables a_{v}, b_{v} or a_{h}, b_{h} only. In this approximation the bubble length l_{bub} is calculated from dividing the bubble volume V_{bub} by the cross-sectional area A occupied by the bubble. For the three possible configurations v, h and c formulas for the bubble length are given below:

$$l_{\text{v}} = \frac{V_{\text{bub}}}{A_{\text{v}}} = \frac{V_{\text{bub}}}{a_{\text{v}}\,b_{\text{v}}} \qquad (8)$$

$$l_{\text{h}} = \frac{V_{\text{bub}}}{A_{\text{h}}} = \frac{V_{\text{bub}}}{a_{\text{h}}\,b_{\text{h}}} \qquad (9)$$

$$l_{\text{c}} = \frac{V_{\text{bub}}}{A_{\text{c}}} = \frac{V_{\text{bub}}}{b_{\text{h}}\,b_{\text{v}} - (b_{\text{h}} - a_{\text{v}})(b_{\text{v}} - a_{\text{h}})}. \qquad (10)$$

2.3 Expressions for the effective surface

In this section expressions for the effective surface are given for the distinct bubble configurations based on Eq. (7). In the configuration where a bubble adopts a vertical position, depicted in Fig. 3a, the effective surface area S_{v} yields:

$$S_{\text{v}} = 2a_{\text{v}}b_{\text{v}} + 2\frac{V_{\text{bub}}}{a_{\text{v}}b_{\text{v}}}\left(a_{\text{h}} + (a_{\text{v}} + b_{\text{v}} - a_{\text{h}})\cos\theta\right) \qquad (11)$$

The first term on the right hand side of Eq. (11) relates to the front and back area of the bubble. The

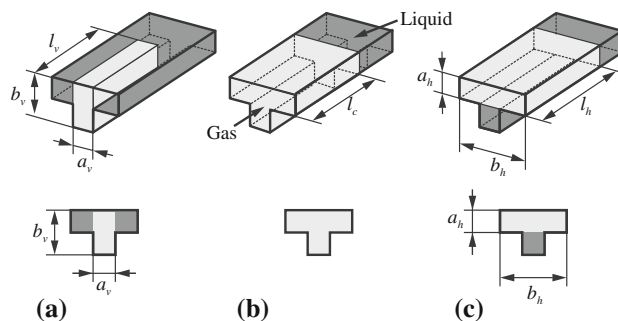**Fig. 3** Possible bubble shape approximations as prisms with the according bubble length: **a** vertical, l_{v}; **b** clogged, l_{c} and **c** horizontal, l_{h}. Corresponding cross-sections are shown below

fraction in the second term denotes the bubble length. In the brackets the first term relates to the liquid gas part and the second term to the solid gas part of the bubbles side area.

The effective area for the horizontal configuration S_h similarly yields:

$$S_h = 2a_h b_h + 2\frac{V_{bub}}{a_h b_h}(a_v + (a_h + b_h - a_v)\cos\theta) \qquad (12)$$

The effective surface area S_c for the clogged configuration finally results in:

$$S_c = 2(a_v b_v + a_h b_h - a_v a_h) \\ + 2\frac{V_{bub}(b_v + b_h)}{(a_v b_v + a_h b_h - a_v a_h)}\cos\theta \qquad (13)$$

2.4 Simplifications for long bubbles and small contact angles

In this section simplifications of the model applicable to many practical cases will be discussed. First, it can be assumed to have bubbles long enough to neglect the front and back areas since they do not contribute significantly to the total surface area of the bubble. Second the contact angle is assumed to be small leading to $\cos\theta \approx 1$. This is a typical value for self filling micro-fluidic structures, e.g. aqueous solutions in glass or silicon based systems with oxidized surfaces. The equations for the effective surface can then be simplified to:

$$\frac{S_v}{V_{bub}} = 2\frac{a_v + b_v}{a_v b_v} \qquad (14)$$

$$\frac{S_h}{V_{bub}} = 2\frac{a_h + b_h}{a_h b_h} \qquad (15)$$

$$\frac{S_c}{V_{bub}} = 2\frac{b_v + b_h}{a_v b_v + a_h b_h - a_v a_h} \qquad (16)$$

In Eqs. (14)–(16) the bubble volume does not contribute to the comparison for determining the bubble configuration anymore. Equations (14)–(16) are anti proportional to the well known hydraulic diameter. Thus there are formulas for the capillary pressure inside the bubble (Finn 1986; Langbein 2002).

2.5 Design scenario

A typical design scenario for a micro-fluidic system is a given maximum depth b_v and maximum width b_h to accommodate a channel. Within this limits a T-shaped channel can be optimized regarding bubble configuration and possible liquid flow rate. Therefore the values of a_v and a_h can be varied and the resulting bubble configurations can be compared. This has been done in Fig. 4 by plotting the separation lines defined by:

$$S_h(a_h, a_v) = S_c(a_h, a_v) \qquad (17)$$

$$S_v(a_h, a_v) = S_c(a_h, a_v) \qquad (18)$$

in the $a_v a_h$-plane. These lines divide the $a_v a_h$-plane into three regions where different bubble configurations are adopted. Figure 4 is calculated for the special case of long bubbles with small contact angles like discussed above. For this simplified case the graphs can be given in an explicit form as relations $a_h(a_v)$. For the line separating the horizontal and the clogged configuration in the $a_v a_h$-plane the expression for $a_h(a_v)$ yields

$$a_h = \frac{a_v b_h}{b_h - a_v}. \qquad (19)$$

Between the vertical and the clogged configuration the relation is given by

$$a_h = \frac{a_v b_v}{a_v + b_v}. \qquad (20)$$

Obviously the last equation only has positive solutions as long as the height of the horizontal configuration a_h is smaller than the total channel depth b_v.

In Fig. 4 the vertical configuration is adopted over a wide range of parameters. This results from the fact that the low aspect ratio of $b_v/b_h = 0.3$ of the enclosing rectangle favours this configuration. In contrast, for aspect ratios of $b_v/b_h > 1$ the horizontal configuration is preferred. For an aspect ratio of $b_v/b_h = 1$ the graph becomes symmetric.

2.6 Varying contact angles

In the general case of arbitrary contact angles and finite bubble length, when solving Eqs. (19) and (20) for $a_h(a_v)$, one obtains large expressions with several distinctions
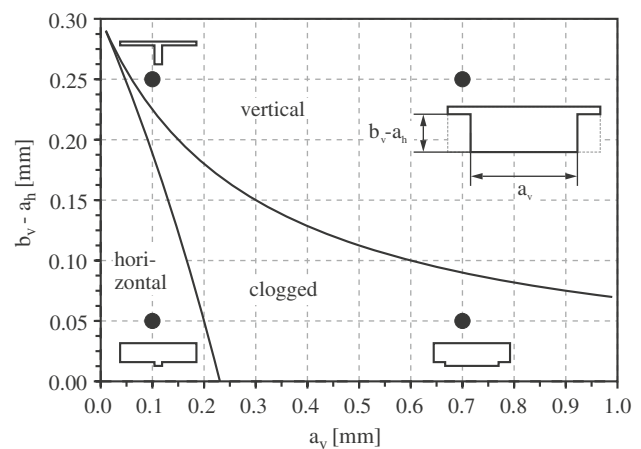

Fig. 4 Separation lines and associated bubble configurations for $b_v = 300\ \mu m$, $b_h = 1,000\ \mu m$. Calculations for long bubbles with $\theta = 0°$ and sketches of the channel geometry at arbitary chosen positions

between regions of definition. Here numerical evaluations of the equations for the considered case $b_v = 300$ μm and $b_h = 1,000$ μm are presented instead. These calculations are performed under the assumption of long bubbles, thus the first terms in Eqs. (11)–(13) are neglected. The results are given in Fig. 5.

A variation of the contact angle from zero towards ninety degrees results in an increasing preference of the system towards the clogged configuration.

2.7 Varying bubble volume

With decreasing bubble length the relative contribution of the bubble caps to the surface energy increases. This is documented in Fig. 6 by numerical evaluation of the bubble shape for different bubble volumes at a constant contact angle of $\theta = 0°$. It is found that smaller bubbles are more likely to adopt the vertical or horizontal configuration than the clogged configuration. In this calculation bubble volumes are denoted by multiples of $b_h^2 b_v$ corresponding to the volume of a bubble in the channel with size $b_h \times b_v$ and length b_h. Figure 6 shows that the approximations made before do not hold for shorter bubbles. However, smaller bubbles tend to prefer a non-clogging configuration compared to longer bubbles. Thus, the approximation made above provides a worst case limit for estimating clogged configurations.

2.8 Comparisons to experiments and simulations

The presented model was compared with experiments performed with a setup described in more detail in Litterst et al. (2004). In these experiments air bubbles have been studied in different Pyrex-covered T-shaped silicon channels filled with water. After priming the channels with
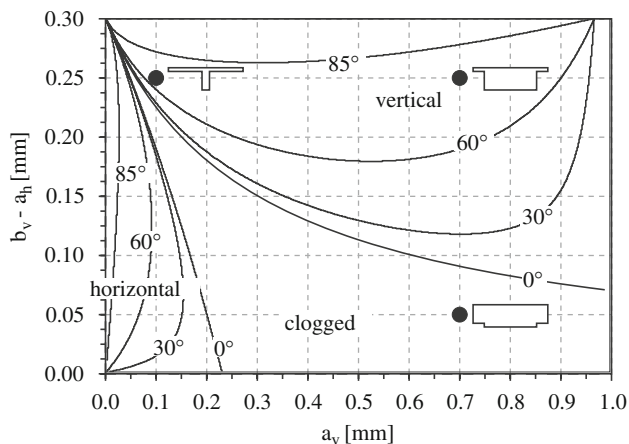
Fig. 5 Separation lines and bubble configurations in dependence of contact angle. ($b_v = 300$ μm, $b_h = 1,000$ μm). Long bubbles are assumed
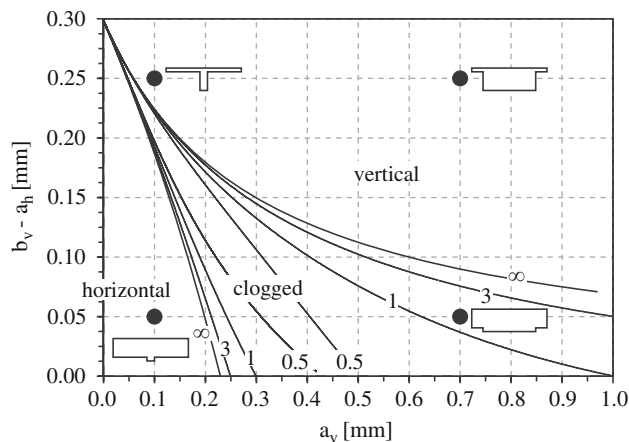
Fig. 6 Separation lines and bubble configurations for different bubble volumes in multiples of $b_h^2 b_v$

deionized water by using a syringe pump, a single air bubble has been injected with a second syringe pump. After sealing the channel with a tape, the bubble configuration has been photographed from the top of the channel. For completion simulations based on computational fluid dynamics (CFD) have been performed to test the validity of the analytical approach. The program used for the simulations is CFD-ACE+ (2004). The adopted bubble configurations in the experiments for $\theta \approx 5°$ as well as for the simulations ($\theta = 5°$) exhibit a good agreements as displayed in Fig. 7. The channels considered in the experiments and simulations have a maximum width and depth of $1,000 \times 300$ μm^2 and varying values of a_v and a_h. To simplify the sizing of the bubble length a scale with a pitch of 500 μm was etched into the silicon samples alongside the channels.

In Fig. 8 the results of the analytical model are plotted for $\theta = 5°$ along with the experimental results and simulated data (symbols). Channel parameters and experimentally observed bubble configurations are depicted in Fig. 9.

While the horizontal and vertical bubble configuration is predicted correctly in all cases the model fails in some cases for the clogged bubble configuration. Since simulation and experimental results agree well in all studied cases, the deviation has to be attributed to the analytical model. A possible reason for this might be the more complex geometry of the clogged bubble configuration and the additional forces acting in the non-convex regions which are not considered in the geometrical approximation of the model.

Nevertheless, the vertical and the horizontal bubble configuration are always predicted correctly. As the deviation from the predicted configuration is always in favour of the technically preferred vertical or horizontal configuration the analytical model provides certainly a worst case estimate whether clogging will occur. Therefore it can be used as a reliable tool for the design of non-clogging channels.

Fig. 7 CFD simulations (*perspective* view) and experimentally obtained photographs (*top* view) of equilibrium bubble configurations; **a** vertical, **b** clogged and **c** horizontal
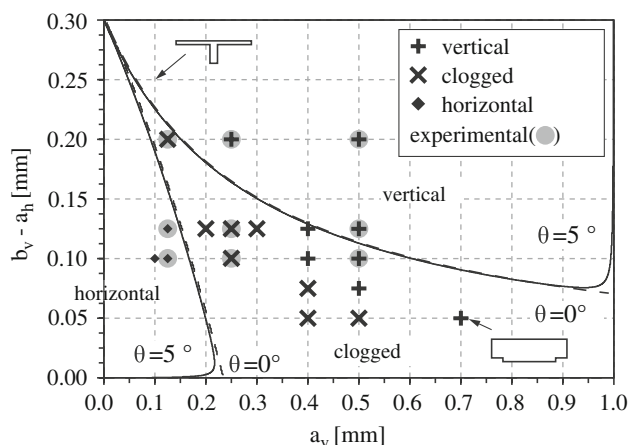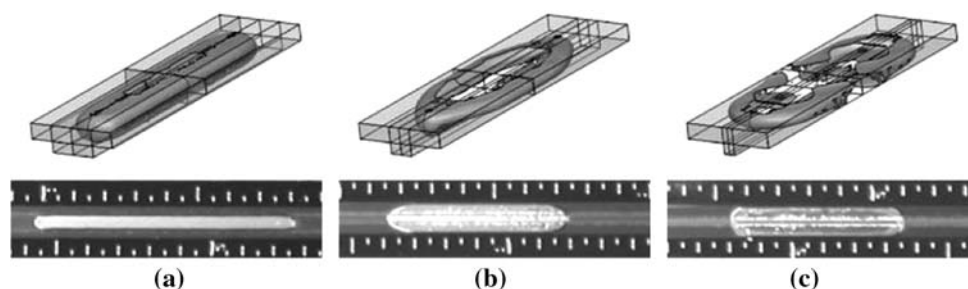

Fig. 8 Experimentally evaluated bubble configurations and results from CFD simulations (*symbols*) compared to model predicted configurations (*separation lines*) for $b_v = 300$ μm; $b_h = 1,000$ μm

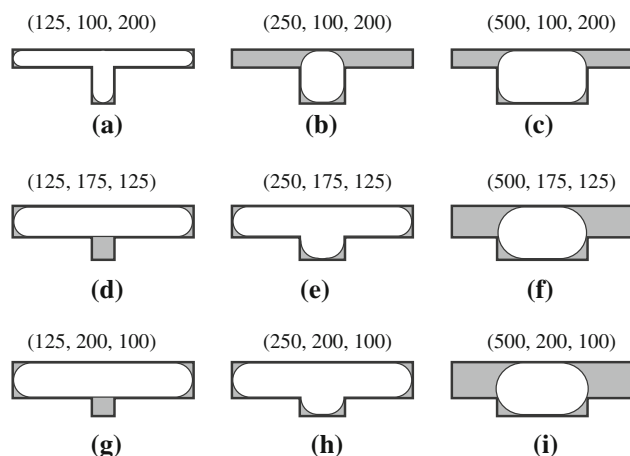**Fig. 9** Sketches of the equilibrium bubble configuration obtained by experiments. The *numbers* in brackets signify a_v, a_h and $b_v - a_h$ in μm, respectively ($b_h = 1,000$ μm; $b_v = 300$ μm)

3 Dynamic bubble behaviour

3.1 Buoyancy driven bubble raise

The separation of liquid and gas in the cross-section of the T-shaped channel enables the liquid to bypass bubbles. In the following the rise velocity of a bubble in a T-shaped

channel subjected to buoyant forces in a vertically arranged channel with sealed ports is investigated. The mean velocity of the liquid bypassing the bubble can be determined by looking at the upward directed gas flow rate Φ_{gas} and the downward vectored liquid flow rate Φ_{liq}. The highest bubble rise velocity is determined for a situation where the flow of the bubble and the liquid are oppositely directed. However, this can be compared with a situation of a stationary bubble and pressure driven liquid bypassing through the side channel. By optimizing the geometry for the highest rise velocity for the oppositely directed movement of gas bubble and liquid the dynamic situation with a rectified movement will show an even better performance. Following the approach of Kohnle et al. (2002) the velocity is given by the balance of both flow rates. Hereby the gas flow rate Φ_{gas} is defined as the rise velocity of the gas bubble multiplied with its cross-sectional area.

The liquid flow rate Φ_{liq} can be predicted from the hydrostatic pressure difference over the bubbles length compared to the fluidic resistance of the liquid filled bypass. Due to the different bubble positions both flow rates have to be defined case sensitive for either the horizontal or the vertical bubble configuration. In case of the blocked channel the liquid flow rate is zero as no part of the channel cross-section is open to the liquid. Flow in the corners or the thin film beside the bubble is orders of magnitude smaller than the flow in an open bypass and is therefore neglected (Wong et al. 1995). For the case of the horizontal bubble configuration the velocity reads as:

$$\bar{v}_h = \frac{\rho g a_v^3 (b_v - a_h)^3}{8\eta(a_v + b_v - a_h)^2 b_h a_h} \tag{21}$$

In case of the vertical bubble configuration two bypasses are formed as shown in Fig. 2a. The two liquid filled channels left and right of the bubble act as a parallel connection of two fluidic resistances in the calculation. This yields a velocity for a vertical bubble configuration of:

$$\bar{v}_v = \frac{\rho g a_h^3 (b_h - a_v)^3}{8\eta a_v b_v (2a_h + b_h - a_v)^2} \tag{22}$$

Equations (21) and (22) are independent of the bubble length. Nevertheless, for "short" bubbles effects like

contact line pinning can dominate. Therefore in experiments the predicted velocity is only observed for sufficiently long bubbles (cf. Kohnle et al. 2002; White and Beardmore 1962).

The predicted bubble velocity is displayed as a contour plot as function of $a_v a_h$ in Fig. 10 for the investigated channel of $b_h = 1,000$ μm width and $b_v = 300$ μm depth. The plot shows huge differences in the velocity between the vertical and the horizontal bubble configuration. The maximum velocity is achieved for the vertical position at the transition line to the clogged channel. The theoretical absolute maximum for the considered case calculates to $v_{max} = 16.87$ mm s^{-1} and is reached for the channel geometry characterized by $a_v = 224$ μm, and $a_h = 128$ μm. Numerically the maximum velocity evaluates for the vertical bubble configuration to be 19 times higher than the maximum velocity in the horizontal bubble configuration for this geometry. The huge difference in the velocity results mainly from the aspect ratio of the embedding structure of 0.3 which is typical for micro-fluidic channels.

3.2 Buoyancy experiments

The model for the bubble buoyancy velocity was verified by experiments with channels like described in Fig. 9 in the previous section. Test samples were fabricated by deep reactive ion etching in silicon and sealed with a Pyrex cover by anodic bonding like reported in Litterst et al. (2004). The media used for all presented experiments are deionized water and air. After priming the channels with water, a single air bubble has been induced with a syringe pump. Then the channel ports have been sealed with tape. The channel has been turned into an upright position and the bubble started to move upwards. A video-camera has been used to study the bubble movement and the video has been analysed later to determine the bubble length and velocity. The experiment has been repeated several times for each bubble in both channel directions and for different bubble sizes.

The results of the buoyancy experiments are summarized in Fig. 11. The velocities obtained in channels (c), (d) and (g) show very good agreement with the analytical

model and stay slightly below the predicted values. The channels (a), (h) and (e) are completely blocked and therefore exhibited no or negligible mobility as expected. For the channels (i), (b) and (f) the experimentally obtained velocity is only half the predicted value. The reason for this is that the length of the test samples did not allow the bubbles to reach the steady state maximum velocity before reaching the end of the sample.

The buoyant velocities obtained in the channels (c), (f) and (i) with bubbles of different size are depicted in Fig. 12 as functions of the bubble length. In case of the channel (c) the experimental values saturate slightly below 2 mm s^{-1}, which means that the maximum velocity is reached within the sample length. For the other samples no saturation could be detected and it can be assumed that the maximum velocity was not reached in these cases. To visualize the fact, that the maximum velocity in samples (f) and (i) could be limited by the sample length (i.e. the maximum bubble length $l_{bub,\ max}$), the data was extrapolated with a linear fit from the origin towards the theoretical bubble velocity. Obviously for the designs (f) and (i) the maximum velocity should be expected for bubbles of around 100 mm length which is far outside the considered experimental sample. Thus, it is most likely that for these cases the maximum velocity was not obtained indeed.

Beside the crude approximation of the gas bubbles as prisms, there are additional drag forces on bubbles as shown, e.g. in Wong et al. (1995, 2005) that may be responsible for some deviation from the presented theory. These effects are independent of the bubbles length (contact angle hysteresis and contact angle dynamics, thin film deposition) but partially dependent on a bubbles velocity (thin film deposition, contact angle dynamics). It is out of scope of this article to quantify such effects as they depend strongly on surface conditions and the actual geometry (Wong et al. 1995, 2005; Bretherton 1961; de Gennes 1985).

Though the maximum predicted velocity for vertical bubbles could not be unambiguously confirmed experimentally for all studied channels, the velocities for the vertical bubbles are in all cases one order of magnitude higher than for the horizontal bubbles. Thus, vertical

Fig. 10 Maximum theoretical velocity v_{max} of gas bubbles in a T-shaped channel as a function of $b_v - a_h$ and a_v at a fixed channel width of 1,000 μm and a total depth of 300 μm. The indices (a) to (i) refer to test samples that have been used for buoyancy experiments (cf. Fig. 9)
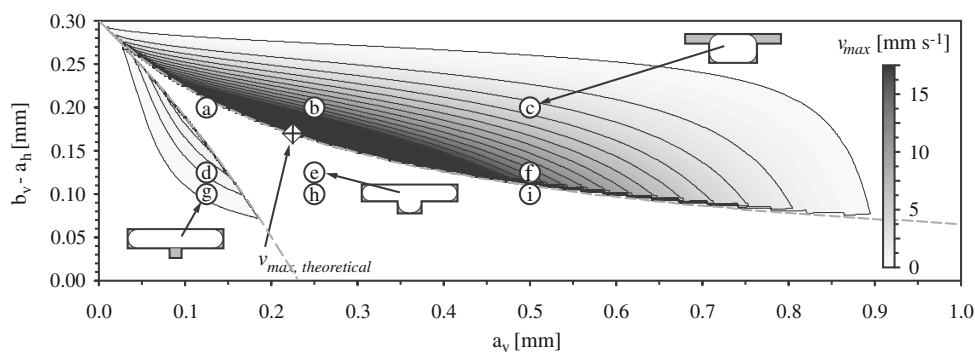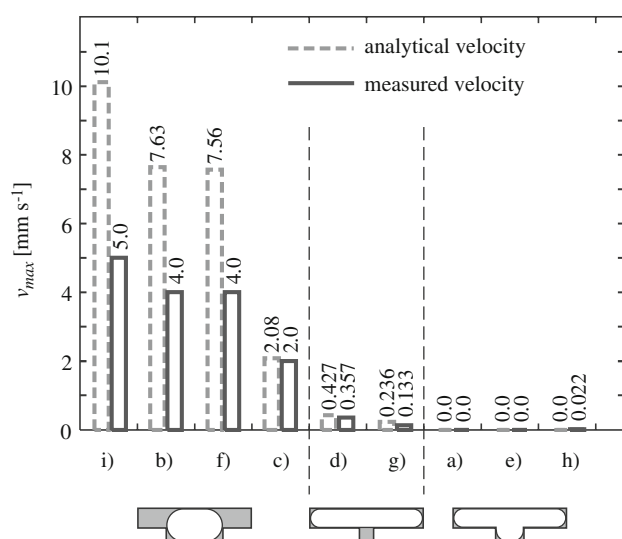
Fig. 11 Measured maximum buoyant velocities of gas bubbles ($l_{bub,max} = 60$ mm) for the various configurations shown in Fig. 10 and in comparison to the analytically predicted maximum velocities
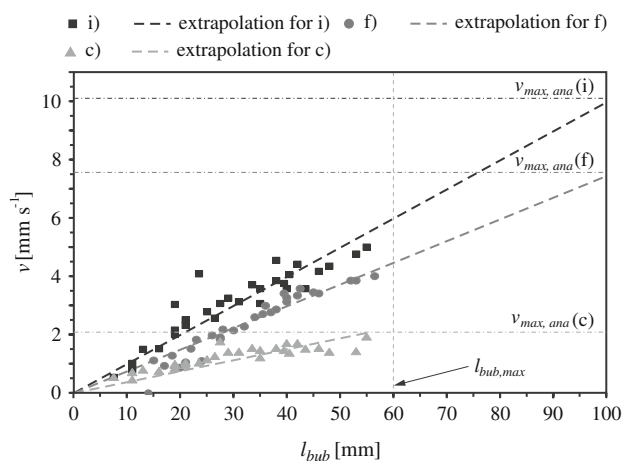

Fig. 12 Measured buoyant velocities for the channels (i), (f) and (c) as function of the bubble length. The experimental data is linearly extrapolated as shown in the graph

bubbles can be considered to be the most favourable configuration to achieve high mobility in T-shaped microchannels of low outer aspect ratio b_v/b_h. The proposed model is able to predict the trend of the velocity magnitude correctly and therefore can be used for optimization of different channel designs to achieve maximum bubble velocity.

3.3 Optimum channel design for highest mobility

In this section the optimum channel design regarding bubble rise velocity is presented. It is derived for any embedding geometry ($b_h \times b_v$) and valid for long bubbles and small contact angles.

Since the highest velocity is achieved for the channel design that provides the lowest fluidic resistance in the bypass channel, the problem scales with the hydraulic diameter of the bypass channels. The maximum hydraulic diameter can be achieved for $b_h \times b_v$ and thus for $a_v = b_h$ and $a_h = b_v$. In this case however, a bubble obtains a clogging configuration. To ensure a non-clogging configuration simultaneously with the maximum velocity of a gas bubble, the design parameters have to be close to the separation line between the non-clogging and the clogging configuration in the $a_v a_h$-plane, because the hydraulic diameter is largest inside the clogged region. To find the absolute maximum, the extreme value

$$\frac{\mathrm{d}}{\mathrm{d}a_v} \bar{v}(a_v, b_h, b_v) = 0 \qquad (23)$$

is evaluated along this graphs. This is done by inserting the expressions for the separation lines Eqs. (19) and (20) into the expressions for the velocities Eqs. (21) and (22). This was done with Mathematica, a computer algebra system (Mathematica® 2006). The calculation is straightforward and leads to large expressions, not given in this manuscript. Here only the results will be shown. For a general description, the length scales are made dimensionless by the horizontal channel extension b_h in the following. The resulting maximum velocities are normalized against $\rho g b_v b_h/(8\eta)$ and plotted in Fig. 13 versus the aspect ratio b_v/b_h. The value used for normalization of the velocities is the virtual velocity a bubble would have in a channel with the enclosing rectangle as cross-section when rising against a liquid flow in a second channel having the same cross-sectional area. This case is purely virtual but it provides an upper limit of the bubble velocity inside the enclosing rectangle. Comparison with this value yields how well the realized channel utilizes the area of the enclosing rectangle.

The corresponding couple's $a_v a_h$ leading to the maximum velocities depicted in Fig. 13 are plotted in Fig. 14. For $b_v/b_h < 0.851$ the maximum velocity is always achieved by channels which lead to vertical bubble configurations while for $b_v/b_h > 0.851$ geometries that exhibit a horizontal configuration achieve the highest velocities.

The lowest maximum velocity is reached for $b_v/b_h = 0.851$. In this case two similar channel configurations exist leading to the same velocity. One exhibits a horizontal and the other a vertical bubble configuration.

To understand the asymmetry of the graph in Fig. 13 one has to take into account that in case of the vertical bubble configuration two bypass channels are built while for the horizontal case only one bypass exists, leading to lower resistance at the same bypass area.

It is remarkable that the maximum achievable bubble velocities increase in general with non-symmetric aspect ratios. The explanation is that with starting from 0.851
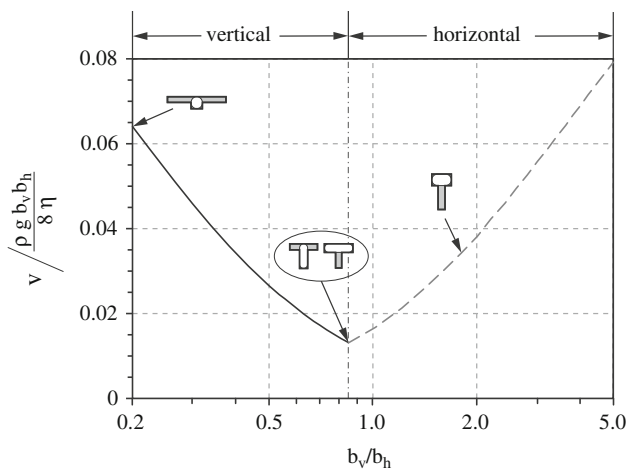
Fig. 13 Maximum normalized bubble velocity for aspect ratios b_v/b_h from 1/5 to 5. For $b_v/b_h = 0.851$ horizontal and vertical bubbles have the same velocity although the underlying geometries differ

increasing or decreasing aspect ratios, the part of the channel profile occupied by the liquid rises much stronger than the part occupied by the bubble. One may think about a T-shaped channel leading to a vertical bubble. The bubble stays vertical even if the total width b_h increases, leading to a smaller flow resistance.

Numerically, an absolute upper limit of 0.148 can be evaluated for the dimensionless normalized velocities. It is predicted for very high (>100) as well as low (<0.01) aspect ratios b_v/b_h. The channel configurations evaluated in Fig. 13 for aspect ratios of up to 5 and down to 1/5 already reach about half of this absolute maximum velocity. Thus, usage of further deformed channels will not increase this value by orders of magnitude.
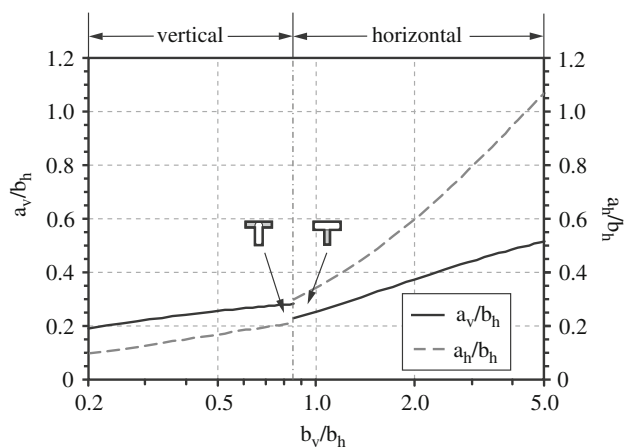

Fig. 14 Design parameters for channels with maximum bubble velocity for any given aspect ratio b_v/b_h from 1/5 to 5. The parameters a_v and a_h can be determined either computationally or read from the graph

The mobility model was derived in the context of buoyancy driven bubbles. Nevertheless, it can be straightforward applied to bubbles driven by centrifugal forces in rotational systems or any other body forces. Also bubbles driven by capillary forces due to electro wetting, the thermo capillary effect or tapering of channels along the axis of movement can be treated in a similar way. In particular, as long as the driving force scales linearly with the bubble length the model should hold without adjustments as the viscous drag scales linearly with the length as well.

4 Conclusions

T-shaped channels are a beneficial alternative to standard micro-channels where micro-fluidic structures have to be kept from clogging by gas bubbles or bubbles have to be transported. For save operation conditions it is essential to design channels leading to the desired non-clogging bubble configurations. The presented analytical model serves this task as it predicts reliably the desired horizontal and vertical bubble configurations. For good wetting conditions with contact angles near zero degree, two simple formulas, Eqs. (19) and (20) are given to decide whether a design leads to a non-clogging configuration or not. For higher contact angles the tendency towards clogging increases. The more complex formulas for the general case can be evaluated numerically or by computer algebra.

The bubble velocity model enables one to compare the bubble velocities in T-shaped channels not only for gravity driven flow but for bubbles driven by various forces. The presented dimensionless maximum velocity describes how efficient the available area is used for the movement of bubbles. In general this value increases for aspect ratios deviating from 0.851 in any direction. For specific optimization purposes one may either take out the best performing channel designs for any aspect ratio from 1/5 to 5 from the presented graphs or solve the equations with computer algebra like described. For typical micro-fluidic designs with low aspect ratios the vertical bubble positions exhibit highest mobility. This has been utilized already in a novel flow field for a direct methanol fuel cell in Litterst et al. (2006). The application of this channel in a direct methanol fuel cell also deals with multiple bubbles and the bubble configuration is correctly described by the presented model also in this case. Furthermore in most cases the bubbles coalesce when they come close together and can then be treated as one as presented here.

References

Bretherton FP (1961) The motion of long bubbles in tubes 2. J Fluid Mech 10(2):166–188

CFD-ACE+, ESI CFD, Inc. (2004) Huntsville, AL. http://esi-group.com, http://www.cfdrc.com

Finn R (1986) Equilibrium capillary surfaces. Springer, Stanford

de Gennes PG (1985) Wetting: statics and dynamics. Rev Mod Phys 57(3):827–863

Goldschmidtboeing F, Rabold M, Woias P (2006) Strategies for void-free liquid filling of micro cavities 1. J Micromech Microeng 16(7):1321–1330

Gravesen P, Braneberg J, Jensen OS (1993) Microfluidics-a review. J Micromech Microeng 3(4):168–182

Jensen MJ, Goranovic G, Bruus H (2002) Dynamics of bubbles in microchannels. In: Proc. of MicroTAS 2002, Nara, Japan, pp 733–735

Jensen MJ, Goranovic G, Bruus H (2004) The clogging pressure of bubbles in hydrophilic microchannel contractions. J Micromech Microeng 14(7):876–883

Kohnle J, Waibel G, Cernosa R, Storz M, Ernst H, Sandmaier H, Strobelt T, Zengerle R (2002) A unique solution for preventing clogging of flow channels by gas bubbles. In: IEEE MEMS, the 15th international IEEE micro electro mechanical conference (ed), Las Vegas, pp 77–80

Langbein D (2002) Capillary surfaces: shape, stability, dynamics, in particular under weightlessness. Springer, New York

Litterst C, Eccarius S, Hebling C, Zengerle R, Koltay P (2006) Increasing μDMFC efficiency by passive CO_2 bubble removal and discontinuous operation. J Micromech Microeng 16(9):S248–S253

Litterst C, Kohnle J, Ernst H, Messner S, Sandmaier H, Zengerle R, Koltay P (2004) Improved gas bubble mobility in CHIC-type flow channels. In: Borgmann H (ed) ACTUATOR. Messe Bremen, Germany, pp 541–544

Mathematica® (2006) Wolfram Research, Inc., Champaign, IL

Steinert CP, Goutier I, Gutmann O, Sandmaier H, Daub M, de Heij B, Zengerle R (2004) A highly parallel picoliter dispenser with an integrated, novel capillary channel structure. Sens Actuators A Phys 116(1):171–177

Steinert CP, Sandmaier H, Daub M, de Heij B, Zengerle R (2004) Bubble-free priming of blind channels. In: Proceedings of IEEE international conference on micro electro mechanical systems, Maastricht, The Netherlands, January 25–29, pp 224–228

The Surface Evolver, Version 2.30, 2008

Waibel G, Kohnle J, Cernosa R, Storz M, Schmitt M, Ernst H, Sandmaier H, Zengerle R, Strobelt T (2003) Highly integrated autonomous microdosage system. Sens Actuators A Phys 103(1–2):225–230

White ET, Beardmore RH (1962) The velocity of rise of single cylindrical air bubbles through liquids contained in vertical tubes. Chem Eng Sci 17(5):351–361

Wong H, Radke CJ, Morris S (1995) The motion of long bubbles in polygonal capillaries. 2. Drag, fluid pressure and fluid–flow 2. J Fluid Mech 292:95–110

Wong H, Radke CJ, Morris S (1995) The motion of long bubbles in polygonal capillaries. 1. Thin-films 1. J Fluid Mech 292:71–94

Wong H, Morris S, Radke CJ (1992) 2-Dimensional menisci in nonaxisymmetric capillaries. J Colloid Interface Sci 148(1):284–287

Wong CW, Zhao TS, Ye Q, Liu JG (2005) Transient capillary blocking in the flow field of a micro-DMFC and its effect on cell performance 1. J Electrochem Soc 152(8):A1600–A1605

Zengerle R, Leitner M, Kluge S, Richter A (1995) Carbon dioxide priming of micro liquid systems. In: Proc. of IEEE-MEMS 1995, Amsterdam, pp 340–343